Performance Analysis of Wavenumber Domain Algorithms for Highly Squinted SAR

Xing Chen, Zhenyu Hou, Zhen Dong, and Zhihua He

***Abstract*—Wavenumber domain algorithms have unique advantages in processing highly squinted synthetic aperture radar data. This article studies the performance of three commonly used wavenumber domain algorithms including the classical wavenumber domain (CWD) algorithm, extended wavenumber domain (EWD) algorithm, and squint wavenumber domain (SWD) algorithm. First, the wavenumber domain signal expression under the zero-Doppler and acquisition-Doppler reference geometries are both derived. Second, the internal relationship between three wavenumber domain algorithms is analyzed. A new interpretation of the relationship between the three algorithms and an interpolation strategy are given. The analysis not only provides a deeper understanding of the three algorithms, but also provides a basis for comparing them. Then, the performance of the three wavenumber domain algorithms is evaluated from the perspectives of computational complexity, image quality, and geometric position through theoretical analysis and simulation experiments. Aiming at the problem that the range and azimuth profiles are not orthogonal, a method to calculate resolution and extract profile is proposed. The results show that all three algorithms can obtain a well-focused images if full-resolution interpolation is performed, and the computational complexities of CWD and SWD are less than that of EWD.**

***Index Terms*—Highly squinted synthetic aperture radar (SAR), stolt mapping, wavenumber domain algorithm.**

I. Introduction

SYNTHETIC aperture radar (SAR), as a unique sensor technology, which provides high-resolution all-weather imaging on a global scale, has been widely used in many civilian and security-related applications [1], [2], [3]. SAR data may be acquired with a squinted geometry, either by design or through platform motion, with squint angles up to several tens of degrees [4]. The highly squinted SAR has the following advantages.

1) Providing information about surface structure through the measurement of the azimuth angle dependence of backscatter [5].
2) Increasing the flexibility with which a desired area on the surface is imaged within a single pass of the platform.
3) Combining with various beam steering imaging modes, such as squinted spotlight [6], squinted sliding spotlight [7], and squinted terrain observation by progressive scans (TOPS) [8], [9], [10].

Compared with the broadside mode, the 2-D coupling of highly squinted SAR signal become more severe with the increase of center squint angle, which makes the imaging processing more complicated [11]. Based on the azimuth translation-invariant property, the frequency/wavenumber domain algorithms can effectively focus the SAR echo [12]. Among them, the range Doppler (RD) algorithm uses the complicated interpolation scheme to accommodate the range and Doppler dependences of both the secondary range compression term and the range cell migration (RCM). As a compromise scheme of efficiency and accuracy, chirp scaling (CS) algorithm is widely used, especially on spaceborne platform [13]. Nevertheless, for high resolution and large squint angle systems, the capabilities of RD and CS algorithms are limited due to approximations. The 2-D coupling can be reduced by the squint-minimization operation [4], [14], [15]. Nonetheless, the RCM and Doppler parameters change along the azimuth after squint-minimization. Many researchers have made improvements to this problem [16], [17], [18], [19]. Unfortunately, these methods have limited ability to handle the variation of Doppler parameters and cannot combined with sliding spotlight and TOPS modes.

By contrast, the wavenumber domain algorithm (also known as omega-K algorithm or range migration algorithm) has unique advantages in processing high-resolution and highly squinted SAR data compared to algorithms described above and is an ideal RCM correction (RCMC) approach without any approximation. The classical wavenumber domain (CWD) algorithm [20], [21] achieves 2-D decoupling compensation by a Stolt mapping in the 2-D wavenumber domain. Then, adaptation called as the extended wavenumber domain (EWD) algorithm has been proposed for airborne case, involving a modified Stolt mapping and including motion compensation [22]. The authors in [23] and [24] adopt the EWD algorithm to focus squinted spotlight SAR data, which is later widely used in squinted sliding spotlight mode [7], [25], squinted TOPS mode [9], and spaceborne squinted SAR [26]. The literature [23] believes that EWD has better focusing effect than CWD when processing squint data, and the processing time of EWD is only 60% of the time of CWD, which is equivalent to the processing time of broadside case. The literature [24] pointed out that the available spectrum support area for CWD is limited in squint mode, which will

Manuscript received 14 November 2022; revised 20 December 2022; accepted 8 January 2023. Date of publication 17 January 2023; date of current version 6 February 2023. This work was supported by the National Natural Science Foundation of China under Grant 61771478 and Grant 42205142. *(Corresponding authors: Zhen Dong; Zhenyu Hou.)*

The authors are with the College of Electronic Science and Engineering, National University of Defense Technology, Changsha 410073, China (e-mail: chenxing13@nudt.edu.cn; houzhenyu11@nudt.edu.cn; dongzhen@nudt.edu.cn; zhihuahe@nudt.edu.cn).

Digital Object Identifier 10.1109/JSTARS.2023.3237552

cause the loss of imaging resolution. Based on the conical reference coordinates, the authors in [27] and [28] proposed the extended EWD algorithm [called squint wavenumber domain (SWD) algorithm in this article for simplicity] to process squinted SAR data. Ping et al. [29] used the SWD to process high squint beam steering SAR, and verified its effectiveness on highly squinted data. The literature [30] rederived the SWD algorithm from the perspective of squint equivalent wavelength and generalized it to the bistatic squinted SAR case. Xiong et al. [30] also pointed out that SWD is more suitable for processing squint SAR than CWD, and only a small part of the support of CWD can be obtained. In conclusion, the wavenumber domain algorithms are widely used to process squinted SAR data, but the existing literature generally believes that CWD is inferior to EWD and SWD in focusing effect and processing efficiency in squint mode. Moreover, to the best of authors' knowledge, the inherent relations or differences between the three algorithms have not been reported yet and the comparative research on the performance of the three algorithms for highly squinted SAR data is relatively limited. Therefore, the motivation of this article is to analyze the performance of these typical algorithms in the squint situation and choose an appropriate solution.

In this article, we analyze the internal relationship of the three wavenumber domain algorithms, and establish an evaluation index system to evaluate their performance. The main contributions can be summarized as follows.

1) A new interpretation of the relationship between the three algorithms and an interpolation strategy are proposed. First, the relationship between different algorithms is analyzed from the perspective of spectrum support area. Then, according to the characteristics of wavenumber domain algorithms, a ratio factor of range wavenumber sizes is defined to describe the interpolation points.
2) The relationship between SWD and CWD in wavenumber domain and image space is deduced through integral transformation. On this basis, this article points out that image obtained by SWD has azimuth tilt, which can be corrected by multiplying a phase function in RD domain. These explanations are original and allow us to have an intuitive understanding of the mappings, geometric positions, and differences of the three algorithms.
3) An evaluation index system is established, including computational complexity, image quality, and geometric position. Aiming at the problem that the range and azimuth profiles are not orthogonal, a method to calculate resolution and extract profile is proposed. Experiments performed on simulation database verify the correctness of the theoretical analysis and are used to analyze the performance of three algorithms.

The rest of this article is organized as follows. Section II establishes the highly squinted SAR signal model and introduces the three wavenumber domain algorithms. Section III analyzes the inherent relations between the three algorithms. A set of evaluation system is presented in Section IV. Imaging experiments are given in Section V. Finally, Section VI concludes this article.

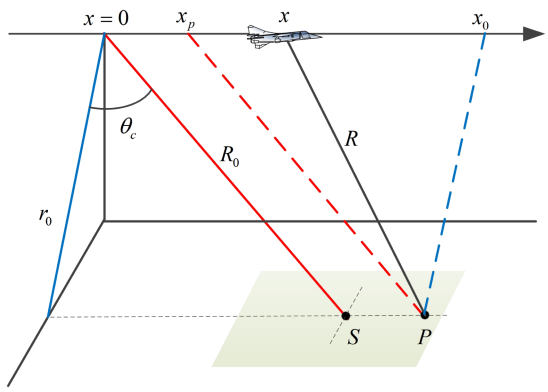

Fig. 1. Acquisition geometry of highly squinted SAR.

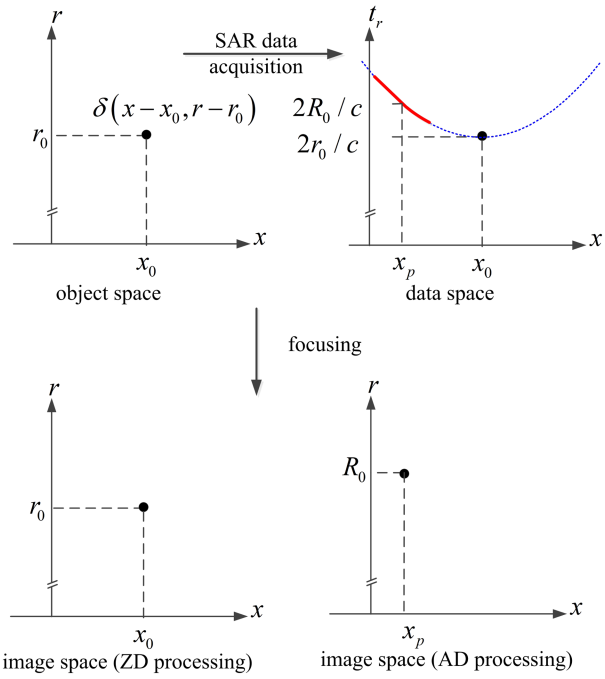

Fig. 2. Coordinate systems used in this article.

II. Overview of Wavenumber Domain Algorithms

A. Signal Model

In this section, we focus on building the signal model for the wavenumber domain methods. The acquisition geometry of highly squinted SAR is shown in Fig. 1. The origin of the azimuth x-axis is taken in the middle of the synthetic aperture interval. θ_c is the beam center squint angle. At the azimuth central time, the beam center illuminates the point S. Point S denotes the scene center and the range from S to radar at θ_c is R_0. Point P denotes a target at the line through S and parallel with the trajectory. The distance between S and P is given by x_p.

We will use the following coordinate systems (see Fig. 2).

1) *Object space:* In the *object space* the location of scatterers is represented as a function of x (azimuth or along-track) and r (slant range or across-track).

2) *Data space:* In the *data space* the received SAR data $ss(x, t_r)$ are represented as a function of x and t_r (fast time). Since t_r is oriented along the wave vector, which is not usually perpendicular to the azimuth, t_r and x are not orthogonal. In this space, the geometric relation is distorted by RCM. As shown in the subgraph in the upper right corner of Fig. 2, the slant range trajectory of the target in the compressed echo space corresponds to the red solid line part.
3) *Image space:* For the focused complex image $u(\cdot)$, two coordinate systems are considered, namely the zero-Doppler (ZD) reference geometry and the acquisition-Doppler (AD) reference geometry [27]. In the ZD reference geometry (also called cylindrical processing geometry), target P is imaged at the range and azimuth position corresponding to an orthogonal geometry (x_0, r_0). r_0 is the closest slant range and x_0 is the azimuth position of target P. In the AD reference geometry (namely the conical processing geometry), target P is imaged at (x_p, R_0). Transformations between the two reference systems are given by

$$\begin{cases} r_0 = R_0 \cos\theta_c \\ x_0 = x_p + R_0 \sin\theta_c \end{cases} \tag{1}$$

where the change of squint angle with the closest slant range is ignored.

Therefore, the instantaneous slant range R can be expressed as

$$\begin{aligned} R(x) &= \sqrt{r_0^2 + (x - x_0)^2} \\ &= \sqrt{(R_0 \cos\theta_c)^2 + (x - x_p - R_0 \sin\theta_c)^2} \end{aligned} \tag{2}$$

where $x = vt_a$ denotes the radar position, v is the equivalent velocity of SAR platform, and t_a is the slow time. SAR image formation is a two-step process: The data acquisition performs the transformation form the object space to the data space and smears out the energy of a single point to a 2-D function $u(\cdot)$, i.e., the point scatterer response. Assume that the transmitted signal is a linear frequency modulation pulse, the demodulated and normalized signal from target P can be written as

$$\begin{aligned} ss(x, t_r) = w_r &\left[t_r - \frac{2R(x)}{c}\right] w_a(x - x_p) \\ &\cdot \exp\left\{j\pi\gamma\left(t_r - \frac{2R(x)}{c}\right)^2\right\} \exp\left\{-j\frac{4\pi f_c}{c}R(x)\right\} \end{aligned} \tag{3}$$

where c denotes the light speed, γ is the chirp rate, and f_c is the carrier frequency. $w_r(\cdot)$ and $w_a(\cdot)$ are the range and azimuth envelops, respectively.

The transfer function in the 2-D wavenumber domain is the basis of the SAR wavenumber domain algorithms. Using the principle of stationary phase (POSP), the signal in the range frequency domain can be expressed as

$$\begin{aligned} sS(x, f_r) = W_r(f_r)\, w_a(x - x_p) &\exp\left(-j\pi\frac{f_r^2}{\gamma}\right) \\ &\cdot \exp\left\{-j\frac{4\pi(f_c + f_r)}{c}R(x)\right\} \end{aligned} \tag{4}$$

As is well known, wavelength $\lambda = c/f_c$ and wavenumbers are linked together by

$$\begin{aligned} k_r &= \frac{4\pi(f_c + f_r)}{c} = k_{rc} + k_{rv} \\ k_x &= \frac{2\pi f_a}{v} = \frac{2\pi(f_{\text{dc}} + f_d)}{v} = k_{xc} + k_{xv} \end{aligned} \tag{5}$$

where k_r denotes the range wavenumber, $k_{rc} = 4\pi f_c/c$ denotes the center of range wavenumber, $k_{rv} = 4\pi f_r/c \in [-2\pi B_r/c, 2\pi B_r/c]$, f_r is the range frequency, B_r is range bandwidth, k_x represents the azimuth wavenumber, $k_{xc} = 2\pi f_{\text{dc}}/v$ represents the Doppler centroid in wavenumber domain, $k_{xv} = 2\pi f_d/v$, f_a is the azimuth frequency, $f_{\text{dc}} = 2v\sin\theta_c/\lambda$ denotes the Doppler centroid, $f_d \in [-B_a/2, B_a/2]$, B_a is the Doppler bandwidth.

The first exponential term in (4) corresponds to range compression, and range matching filtering can be obtained by multiplying $\exp(j\pi f_r^2/\gamma)$. Then, azimuth fast Fourier transform (FFT) is applied to achieve the 2-D spectral expression, which gives

$$SS(k_x, k_r) = \int sS(x, f_r) \exp(-jk_x x)\, dx \tag{6}$$

Substituting the first row of (2) into (6) and using POSP again. The first derivative of the phase function with respect to x is set to zero as

$$k_r \frac{x - x_0}{\sqrt{r_0^2 + (x - x_0)^2}} + k_x = 0 \tag{7}$$

Solving the abovementioned equation, the stationary phase point yields

$$x^* = -\frac{k_x}{\sqrt{k_r^2 - k_x^2}} r_0 + x_0 \tag{8}$$

Replace x in (6) with x^*, and the 2-D spectral expression can be derived as

$$SS(k_x, k_r) = W_r(k_r)\, W_a(k_x - k_{xc}) \exp\{j\Phi_0(k_x, k_r)\} \tag{9}$$

with

$$\Phi_0(k_x, k_r) = -r_0\sqrt{k_r^2 - k_x^2} - k_x x_0 \tag{10}$$

in the ZD geometry. $W_r(\cdot)$ and $W_a(\cdot)$ denotes the range and azimuth envelops in the wavenumber domain, respectively. Similarly, using (1), the phase in the AD geometry is rewritten as

$$\Phi_0(k_x, k_r) = -R_0\cos\theta_c\sqrt{k_r^2 - k_x^2} - k_x R_0 \sin\theta_c - k_x x_p \tag{11}$$

Equations (10) and (11) are the core of SAR imaging algorithms. Obviously, the expression in the AD geometry is consistent with that in the ZD geometry when the squint angle is zero.

B. Wavenumber Domain Algorithms

1) CWD: The CWD algorithm is performed based on the ZD geometry, i.e., (10). The first focusing step of the CWD algorithm is a reference function multiply (RFM) implemented in the 2-D wavenumber domain. The phase of RFM filter equals to

$$\Phi_{\text{ref}}(k_x, k_r) = r_{\text{ref}}\sqrt{k_r^2 - k_x^2} \tag{12}$$

where r_{ref} refers to the reference closest slant range. After the RFM filtering, the phase remaining is given by

$$\Phi_{\text{RFM}}(k_x, k_r) = -(r_0 - r_{\text{ref}})\sqrt{k_r^2 - k_x^2} - k_x x_0 \tag{13}$$

Using the RFM filter has the effect of canceling the phase at the reference range, which focuses the data correctly at that range. The need now is to focus the targets at other ranges. This is done by a mapping of the range wavenumber axis, using an interpolator developed by Stolt. The conventional Stolt mapping (CSM) can be written as

$$k_y = \sqrt{k_r^2 - k_x^2} \tag{14}$$

After the CSM, the phase function of compressed signal becomes

$$\Phi_{\text{CSM}}(k_x, k_y) = -(r_0 - r_{\text{ref}})k_y - k_x x_0 \tag{15}$$

Using 2-D inverse FFT (IFFT), the target will be well focused and correctly registered.

2) EWD: The RFM operation of the EWD algorithm is the same as (12). However, a modified Stlot mapping (MSM) is adopted, i.e.,

$$k_{yE} = \sqrt{k_r^2 - k_x^2} - \sqrt{k_{rc}^2 - k_x^2} + k_{rc} \tag{16}$$

After the MSM, the phase in 2-D wavenumber domain becomes

$$\Phi_{\text{MSM}}(k_x, k_{yE}) = -(r_0 - r_{\text{ref}}) \cdot \left(\sqrt{k_{rc}^2 - k_x^2} + k_{yE} - k_{rc}\right) - k_x x_0 \tag{17}$$

It can be seen that MSM only accomplishes residual RCMC and residual range-azimuth coupling compensation. Comparing (17) with (15) shows that an unwanted phase term is present and can be eliminated in RD domain. Using range IFFT, the signal phase in RD domain can be expressed as

$$\Phi_1(k_x, r_0) = -(r_0 - r_{\text{ref}})\left(\sqrt{k_{rc}^2 - k_x^2} - k_{rc}\right) - k_x x_0. \tag{18}$$

Therefore, residual azimuth compression (AC) phase function can be obtained as

$$\Phi_{\text{AC}}(k_x, r_0) = (r_0 - r_{\text{ref}})\left(\sqrt{k_{rc}^2 - k_x^2} - k_{rc}\right) \tag{19}$$

Finally, the focused image is obtained after azimuth IFFT processing.

3) SWD: The SWD algorithm is derived in the AD geometry. In (11), the first term represents the range-azimuth coupling, the second term represents the azimuth offset caused by the squinted geometry, and the third term denotes the position of the target relative to the azimuth center. The bulk focusing filter in SWD algorithm equals to

$$\Phi_{\text{ref,S}}(k_x, k_r) = R_{\text{ref}}\left(\cos\theta_c\sqrt{k_r^2 - k_x^2} + k_x \sin\theta_c\right) \tag{20}$$

where $R_{\text{ref}} = r_{\text{ref}}/\cos\theta_c$ denotes the reference slant range. Compared with (12), there is one more item $k_x \sin\theta_c$ in (20), which is used to compensate the center phase shift of the echo caused by the squinted geometry. The residual phase in the 2-D wavenumber domain becomes

$$\Phi_{\text{RFM,S}}(k_x, k_r) = -(R_0 - R_{\text{ref}}) \cdot \left(\cos\theta_c\sqrt{k_r^2 - k_x^2} + k_x \sin\theta_c\right) - k_x x_p \tag{21}$$

Then, a new frequency mapping function called as squinted Stolt mapping (SSM) can be obtained as

$$k_{yS} = \cos\theta_c\sqrt{k_r^2 - k_x^2} + k_x \sin\theta_c \tag{22}$$

After the SSM, the phase function of the compressed signal becomes

$$\Phi_{\text{SSM}}(k_x, k_{yS}) = -(R_0 - R_{\text{ref}})k_{yS} - k_x x_p \tag{23}$$

Finally, the focused image is obtain by 2-D IFFT.

III. Relations Between the Wavenumber Domain Algorithms

A. Spectral Support Area

The main difference between the three algorithms is the mapping. Therefore, in order to deeply understand the inherent connections of the three algorithms, the mapping relationships are analyzed. Since both the EWD and SWD have evolved from the CWD, the CWD serves as the basis for our analysis.

Fig. 3(a) illustrates the range wavenumber of raw data as a function of the azimuth wavenumber. Gray area indicates the spectral support area. In the 2-D wavenumber domain, the Doppler wavenumber varies with the range wavennumber, and the relation can be expressed as

$$k_x = k_r \sin\theta \tag{24}$$

where θ is the instantaneous squint angle. The size of range wavenumber is $S_r = k_{r,\max} - k_{r,\min} = 4\pi B_r/c$, $k_{r,\max} = 4\pi(f_c + B_r/2)/c$, $k_{r,\min} = 4\pi(f_c - B_r/2)/c$. The spectrum of the echo is tilted along the azimuth direction. The width of the azimuth wavenumber is $[k_{x,\min}, k_{x,\max}]$, $k_{x,\max} = k_{r,\max}\sin(\theta_c + \theta_a/2)$, $k_{x,\min} = k_{r,\min}\sin(\theta_c - \theta_a/2)$. θ_a represents the azimuth beam width. It should be clearly pointed out that the spectrum support area is calculated according to the range bandwidth B_r and azimuth bandwidth B_a, rather than the range sampling frequency and pulse repetition frequency (PRF).

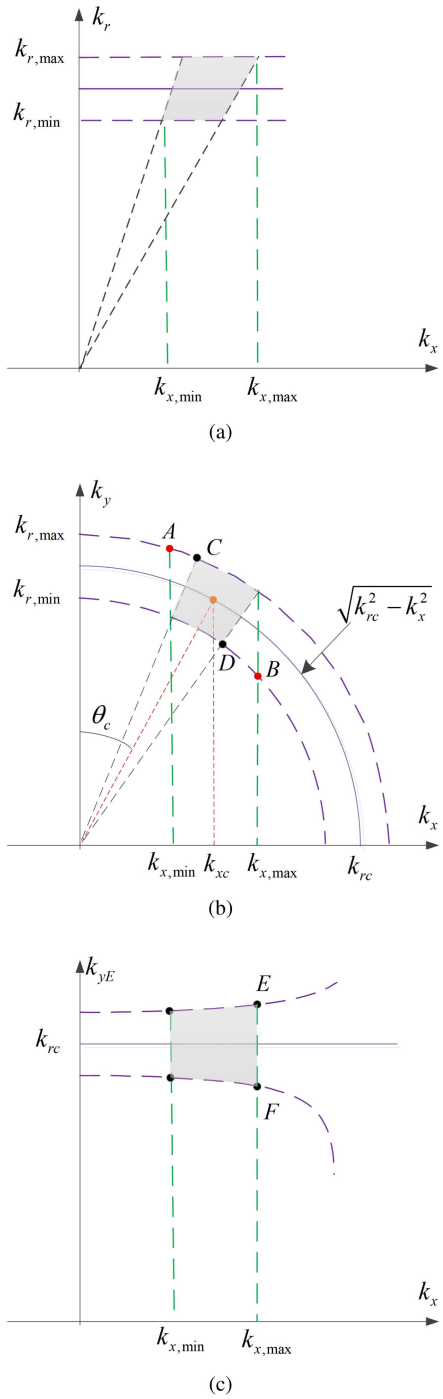

Fig. 3. Signal spectrum in squint mode. (a) Raw data. (b) After the CSM. (c) After the MSM.

The Doppler bandwidth can be represented as

$$B_a = \frac{v}{2\pi}\left(k_{x,\max} - k_{x,\min}\right) \approx \frac{2v}{L_a}\cos\theta_c + \frac{2vB_r}{c}\sin\theta_c = B_{\text{bf}} + B_{\text{sq}} \tag{25}$$

Equation (25) indicates that the Doppler bandwidth in the squint case consists of the beam footprint bandwidth B_{bf} and the squinted bandwidth B_{sq}. L_a is the azimuth antenna size. In the highly squinted case, B_a is much larger than B_{bf}. To avoid azimuth aliasing, the system requires a high PRF. If the sampling frequency is set as slightly greater than B_{bf}, the azimuth upsampling processing can be used. Details can be found in the literature [31].

The spectral support regions after the CSM and MSM are shown in Fig. 3(b) and (c). As can be seen from Fig. 3(b), the CSM results in a skewing and a downward shifting of the data spectrum. The authors in [23] and [24] used the width of range wavenumber corresponding to points A and B for interpolation, namely

$$S_{y,\text{CSM1}} = \sqrt{k_{r,\max}^2 - k_{x,\min}^2} - \sqrt{k_{r,\min}^2 - k_{x,\max}^2} \tag{26}$$

At this time, it is noted that the size of the data spectrum in the range wavenumber direction increases significantly. In fact, the effective width of range wavenumber is the interval between points C and D, which can be expressed as

$$S_{y,\text{CSM2}} = k_{r,\max}\cos\left(\theta_c - \theta_a/2\right) - k_{r,\min}\cos\left(\theta_c + \theta_a/2\right) \tag{27}$$

There is no doubt that $S_{y,\text{CSM2}}$ is much smaller than $S_{y,\text{CSM1}}$.

A first-order Taylor expansion of (14) at k_{rc} along the range wavenumber is as follows:

$$\sqrt{k_r^2 - k_x^2} = \sqrt{k_{rc}^2 - k_x^2} - \frac{k_{rc}}{\sqrt{k_{rc}^2 - k_x^2}}k_{rv} \tag{28}$$

The first term in (28) represents the residual azimuth modulation. The second term denotes the residual RCM. The higher order range-azimuth coupling terms are ignored here. These terms are mixed in (14), and are corrected simultaneously by the CSM. The skew and shift effect of the CSM mainly results from the residual azimuth modulation term $\sqrt{k_{rc}^2 - k_x^2}$, which corresponds to the purple solid circle line in Fig. 3(b). Obviously, if the purple solid line is subtracted at each azimuth position [corresponding the MSM in (16)], the skew and downward of the spectrum can be avoided, as shown in Fig. 3(c). Therefore, for the squinted SAR, this operation offers two benefits: On the one hand, the downward shift and skew of the spectrum are corrected. On the other hand, this term corresponds to the residual AC, which can be compensated in the RD domain, and easily combined with the classical two-step motion compensation method. At this time, the size of range wavenumber is the interval between points E and F, and can be represented as

$$S_{y,\text{MSM}} = \sqrt{k_{r,\max}^2 - k_{x,\max}^2} - \sqrt{k_{r,\min}^2 - k_{x,\max}^2} \tag{29}$$

Compared to the CSM, an extra precondition that should be satisfied in the MSM is $k_{x,\max} \leqslant k_{rc}$, which guarantees that the azimuth modulation term will not get complex values at the overall azimuth wavenumber.

As mentioned above, the residual azimuth modulation term in (28) corresponds to the skew and shift of the spectrum. Expanding this term at the Doppler center wavennumber k_{xc},

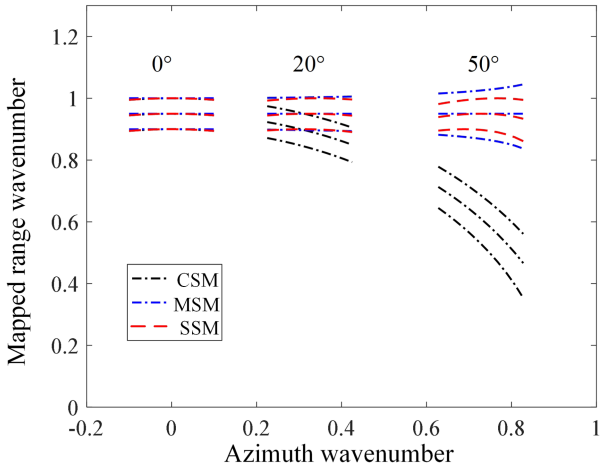

Fig. 4. CSM, MSM, and SSM as functions of azimuth wavenumber.

we have

$$\sqrt{k_{rc}^2-k_x^2}\approx\sqrt{k_{rc}^2-k_{xc}^2}-\frac{k_{xc}}{\sqrt{k_{rc}^2-k_{xc}^2}}\left(k_x-k_{xc}\right)-\frac{k_{rc}^2}{2\left(k_{rc}^2-k_{xc}^2\right)^{3/2}}\left(k_x-k_{xc}\right)^2 \tag{30}$$

In the broadside case, the linear term in (30) equals to zero, and only the quadratic term remains. However, for the highly squinted SAR, the linear term is dominant and the spectrum skewing is approximately linear. As shown in Fig. 3(b), based on the geometric relation, we obtain

$$\frac{k_{xc}}{\sqrt{k_{rc}^2-k_{xc}^2}}=\tan\theta_c \tag{31}$$

Combining (30) and (31) and ignoring quadratic terms, (31) can be rewritten as

$$\sqrt{k_{rc}^2-k_x^2}\approx\sqrt{k_{rc}^2-k_{xc}^2}+k_{xc}\tan\theta_c-k_x\tan\theta_c \tag{32}$$

The first and second terms are constants. The third term $k_x\tan\theta_c$ is the main factor of spectrum distortion. Defining a new mapping relationship

$$k_{y1}=\sqrt{k_r^2-k_x^2}+k_x\tan\theta_c \tag{33}$$

This mapping separates the spectrum distortion term in (30), so that the mapped spectrum support area is without significant skewing. The relationship between k_{y1} and k_{yS} is

$$k_{yS}=k_{y1}\cos\theta_c \tag{34}$$

Therefore, it is known that SSM corresponds to the skew and scale transformations of CSM. Since the SSM is related to the central squint angle θ_c, the corresponding spectral support area of the SSM cannot be obtained directly and must be calculated according to the specific squint angle value. In order to intuitively compare the three mapped spectrums, we used numerical simulation to quantitatively compare the variation of mapped range wavemuber with azimuth wavenumber at 0°, 20°, and 50° squint angles. The results are shown in Fig. 4. Set the parameter $k_r'=k_r/k_{r,\max}\in[k_{r,\min}/k_{r,\max},1]=[0.9,1]$. At the 0° squint case, the spectral support regions of different mappings are approximately the same. With the increase of squint angle, the support areas gradually becomes larger, but the support area of SSM always remains the minimum. The size of range wavenumber after SSM is given by

$$S_{y,\mathrm{SSM}}=\max\left(k_{yS}\right)-\min\left(k_{yS}\right). \tag{35}$$

Indeed, the interpolation is performed on the range direction and the width of mapped spectral support region determines the number of interpolation points. Defining the ratio factor

$$\alpha=S_y/S_r \tag{36}$$

where S_r and S_y represent the range wavenumber sizes before and after mapping, respectively. It should be pointed out that S_r and S_y are calculated according to the range bandwidth B_r and azimuth bandwidth B_a of the signal. There is a certain oversampling in the actual echo data. If the range oversampling factor is σ_r, the number of interpolation points required can be expressed as

$$N_y=\begin{cases}\left(\alpha/\sigma_r\right)N & \alpha>\sigma_r\\ N & \alpha\leqslant\sigma_r\end{cases} \tag{37}$$

where N is the range sampling points of echo. It can be seen from (37) that when the ratio factor is less than the range oversampling factor, the entire spectrum support area can be covered without expanding the interpolation points.

B. Image Space Signal

Next, we will focus on the image space signals after the different mappings. It can be seen from (15) and (19) that target P is focused at position (x_0,r_0) in image domain after the CWD and EWD processing, which means that the echo is aligned to its ZD position. Comparing (12) and (20), we can see that if phase $k_x r_{\mathrm{ref}}\tan\theta_c$ is added to (12), the two formulas are equivalent. This phase is mainly used to correct the center offset caused by squint geometry. After introducing this item, target P will be focused on $(x_0-r_{\mathrm{ref}}\tan\theta_c,r_0)$ after the CWD and EWD processing.

The relationship between CSM and SSM can be expressed in the following matrix form:

$$\begin{bmatrix}k_x\\ k_{yS}\end{bmatrix}=\begin{bmatrix}1 & 0\\ \sin\theta_c & \cos\theta_c\end{bmatrix}\begin{bmatrix}k_x\\ k_y\end{bmatrix}. \tag{38}$$

Let $\mathbf{f_1}=[k_x,k_{yS}]^{\mathrm{T}}$, $\mathbf{f}=[k_x,k_y]^{\mathrm{T}}$, $\mathbf{H}=[1,0;\sin\theta_c,\cos\theta_c]$. The image space signals of the two transformations can be represented as [corresponding to the 2-D IFFT of (15) and (23)]

$$u\left(\mathbf{t}\right)=\int SS\left(\mathbf{f}\right)\exp\left(j\mathbf{t}\cdot\mathbf{f}\right)d\mathbf{f} \tag{39}$$

$$u\left(\mathbf{t_1}\right)=\int SS\left(\mathbf{Hf}\right)\exp\left(j\mathbf{t}\cdot\mathbf{f}\right)d\mathbf{f} \tag{40}$$

where $\mathbf{t}=[x_0,r_0]^{\mathrm{T}}$, $\mathbf{t_1}=[x,r]^{\mathrm{T}}$, $d\mathbf{f}=dk_xdk_y$, $SS(\mathbf{f})=\exp\{j\Phi_{\mathrm{CSM}}(\mathbf{f})\}$, $SS(\mathbf{Hf})=\exp\{j\Phi_{\mathrm{SSM}}(\mathbf{f_1})\}$. The following

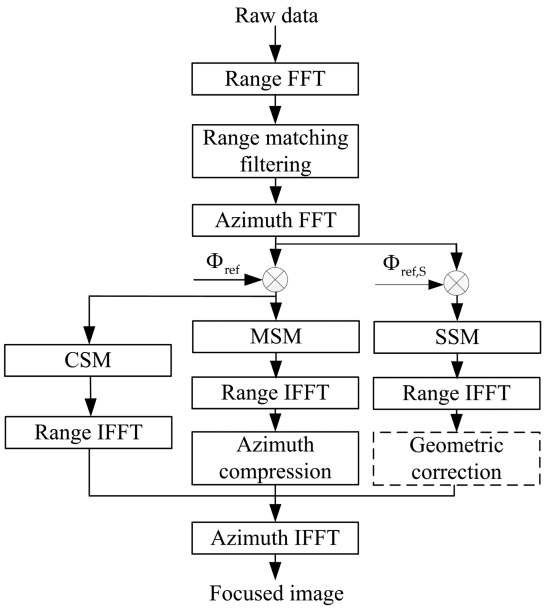

Fig. 5. Block diagram of the three algorithms.

formula can be obtained:

$$\begin{aligned}\mathbf{t}\cdot\mathbf{f}&=\mathbf{t}\cdot\left(\mathbf{H}^{-1}\mathbf{f_1}\right)=\mathbf{t}^{\mathrm{T}}\mathbf{H}^{-1}\mathbf{f_1}\\&=\left(\left(\mathbf{t}^{\mathrm{T}}\mathbf{H}^{-1}\right)^{\mathrm{T}}\right)^{\mathrm{T}}\mathbf{f_1}=\left(\mathbf{H}^{-\mathrm{T}}\mathbf{t}\right)\cdot\mathbf{f_1}\end{aligned}\tag{41}$$

Substituting (38) into (37), we get

$$\begin{aligned}u\left(\mathbf{t_1}\right)&=\int SS\left(\mathbf{Hf}\right)\exp\left(j\mathbf{t}\cdot\mathbf{f}\right)d\mathbf{f}\\&=\int SS\left(\mathbf{f_1}\right)\exp\left(j\mathbf{H}^{-\mathrm{T}}\mathbf{t}\cdot\mathbf{f_1}\right)\frac{d\mathbf{f_1}}{|\det\mathbf{H}|}\\&=\frac{1}{|\det\mathbf{H}|}u\left(\mathbf{H}^{-\mathrm{T}}\mathbf{t}\right)\end{aligned}\tag{42}$$

and

$$\mathbf{t_1}=\mathbf{H}^{-\mathrm{T}}\mathbf{t}=\left(x_0-r_0\tan\theta_c,r_0/\cos\theta_c\right)^{\mathrm{T}}\tag{43}$$

Therefore, for the point target P that is focused to (x_0,r_0) in CWD, it is focused to $(x_0-r_0\tan\theta_c,r_0/\cos\theta_c)=(x_0-R_0\sin\theta_c,R_0)$ after the SSM. In fact, the squint angle in (1) varies with the closest slant range r_0. Obviously, for targets located at different slant range, there is a different offset in the azimuth direction, which makes the focused image tilt, but does not affect the focus quality. The tilt of the image along azimuth can be corrected by multiplying the phase in the RD domain as follows:

$$H\left(k_x,R_0\right)=\exp\left(-jk_x\left(R_0-R_{\mathrm{ref}}\right)\sin\theta_c\right)\tag{44}$$

At this point, the tilt effect of the image is corrected and the target is focused to $(x_0-r_{\mathrm{ref}}\tan\theta_c,R_0)$. Based on the above-mentioned analysis, the block diagram of the three algorithms is shown in Fig. 5. The proposed geometric correction method is represented by a dashed box.

IV. Evaluation Metrics

To compare the performance of the three algorithms, an evaluation system is established in this section.

A. Computational Complexity

Computational complexity is an important indicator to measure the practicality of an algorithm. In theory, this is usually evaluated by computing the floating point operations (FLOPs) of the main steps. Let the size of echo data be $M\times N$ (azimuth and range). An FFT operation on N-point complex data requires $5N\log_2N$ FLOPs, and a complex multiplication operation requires 6 FLOPs. As shown in Fig. 5, the computational complexity of the three algorithms before mapping is equal and can be expressed as

$$C_{\mathrm{com}}=M\cdot5N\log_2N+N\cdot5M\log_2M+6MN\tag{45}$$

After mapping, the new samples are not equally sampled and interpolation is required to allow IFFT processing. The selection of the interpolator is critical for the final image quality and no simple and cheap interpolator will do. Here, we choose the $\mathrm{sinc}(\cdot)$ interpolation kernal function. Let the length of the interpolation kernel be S_{ker}, then the complexity of interpolating a complex data is $2(2S_{\mathrm{ker}}-1)$ FLOPs. Thus, the FLOPs amount of the interpolation operation can be expressed as $M\cdot2N_y(2S_{\mathrm{ker}}-1)$. Therefore, the computational complexity of the three algorithms are given by

$$\begin{aligned}C_{\mathrm{CWD}}&=C_{\mathrm{com}}+M\cdot2N_{y,\mathrm{CWD}}\left(2S_{\mathrm{ker}}-1\right)\\&\quad+M\cdot5N_{y,\mathrm{CWD}}\log_2N_{y,\mathrm{CWD}}+N_{y,\mathrm{CWD}}\cdot5M\log_2M\end{aligned}\tag{46}$$

$$\begin{aligned}C_{\mathrm{EWD}}&=C_{\mathrm{com}}+M\cdot2N_{y,\mathrm{EWD}}\left(2S_{\mathrm{ker}}-1\right)\\&\quad+M\cdot5N_{y,\mathrm{EWD}}\log_2N_{y,\mathrm{EWD}})+N_{y,\mathrm{EWD}}\cdot5M\log_2M\\&\quad+6MN_{y,\mathrm{EWD}}\end{aligned}\tag{47}$$

$$\begin{aligned}C_{\mathrm{SWD1}}&=C_{\mathrm{com}}+M\cdot2N_{y,\mathrm{SWD}}\left(2S_{\mathrm{ker}}-1\right)\\&\quad+M\cdot5N_{y,\mathrm{SWD}}\log_2N_{y,\mathrm{SWD}}+N_{y,\mathrm{SWD}}\cdot5M\log_2M\end{aligned}\tag{48}$$

$$\begin{aligned}C_{\mathrm{SWD2}}&=C_{\mathrm{com}}+M\cdot2N_{y,\mathrm{SWD}}\left(2S_{\mathrm{ker}}-1\right)\\&\quad+M\cdot5N_{y,\mathrm{SWD}}\log_2N_{y,\mathrm{SWD}}+N_{y,\mathrm{SWD}}\cdot5M\log_2M\\&\quad+6MN_{y,\mathrm{EWD}}\end{aligned}\tag{49}$$

where $N_{y,\mathrm{CWD}}$, $N_{y,\mathrm{EWD}}$, $N_{y,\mathrm{SWD}}$ correspond to the interpolation points of the CWD, EWD, and SWD, respectively. C_{SWD1} and C_{SWD2} represent the calculation amount with and without geometric correction, respectively. It can be seen that if the same range wavenumber width is selected for interpolation, the computational complexity of the three algorithms can be approximately the same. However, in order to obtain a full-resolution image, interpolation is required based on the size of the mapped support region.

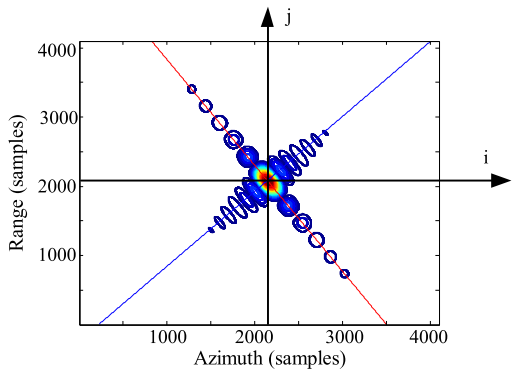

Fig. 6. 2-D contour diagram of squint SAR.

B. Image Quality

The quality of the focused image is the most important indicator for evaluating the performance of the algorithm. For SAR systems, it is obtained by measuring the system response of isolated scattering points. The metrics parameters include:

1) resolution (Res);
2) peak sidelobe ratio;
3) integrated sidelobe ratio (ISLR).

Among them, the assessment of resolution is particularly important.

In the broadside mode, the range and azimuth profiles of the 2-D SAR image can be considered perpendicular to each other and parallel to the coordinate axis. Let the peak position be (i_c, j_c). i and j indicate the azimuth and range coordinate index, respectively. The azimuth and range sampling intervals are d_a and d_r. At this time, the row vector (i, j_c) represents the azimuth profile data, and the column vector (i_c, j) represents the range profile data. The 3 dB mainlobe width of the azimuth and range profiles corresponds to n_a and n_r sampling points, respectively. Then, the azimuth and range resolution can be expressed as

$$\begin{cases} \rho_a = n_a \cdot d_a \\ \rho_r = n_r \cdot d_r. \end{cases} \tag{50}$$

However, the range and azimuth profiles are nonorthogonal in highly squinted SAR. Thus, the profiles cannot be extracted in either horizontal or vertical lines. Fig. 6 shows the 2-D upsampled image obtained by EWD at 50° squint angle. The red solid line represents the extraction line of azimuth profile, and the blue solid line indicates the extraction line of the range profile. The range and azimuth signals can only be completely obtained by extracting along the red and blue lines. Therefore, we propose a method for target profile extraction and resolution calculation for squinted SAR, which is described as follows.

The peak position (i_c, j_c) is taken as the coordinate origin to establish the coordinate system, as shown in Fig. 6. For the squinted SAR system, the scope of the squint angle satisfies $\theta_c \in (0, \pi/2)$. Thus, the azimuth extraction line is located in the II and IV quadrants, and the range extraction line lies within the I and III quadrants. For the azimuth profile, another point $(i_{\text{sub},a}, j_{\text{sub},a})$ along the red line is first obtained. The slope of the red line is $l_a = (j_c - j_{\text{sub},a})/(i_c - i_{\text{sub},a})$ and $\vartheta_a = \text{atan}(l_a)$. $\vartheta_a \in (-\pi/2, 0)$ denotes the inclination angle. For different interpolation points and different squint angles, there are two extraction situations, namely, either by each row or by each column.

Case 1: $-\pi/2 < \vartheta_a \leqslant -\pi/4$. Because there are some columns without red line passing by, the azimuth profile needs to be extracted along each row j, and can be expressed as $u[\text{round}(i_1), j]$. $i_1 = (j - j_c)/l_a + i_c$. The round$(\cdot)$ operation denotes the rounding of the numerical values.

Case 2: $-\pi/4 < \vartheta_a < 0$. The azimuth profile needs to be extracted along each column i and can be written as $u[i, \text{round}(j_1)]$. $j_1 = l_a(i - i_c) + j_c$. Therefore, the azimuth resolution can be expressed as

$$\begin{cases} \rho_a = n_a\sqrt{d_r^2 + (d_a/l_a)^2}, \text{Case1} \\ \rho_a = n_a\sqrt{d_a^2 + (l_a d_r)^2}, \text{Case2}. \end{cases} \tag{51}$$

Similarly, for the range profile, another point $(i_{\text{sub},r}, j_{\text{sub},r})$ along the blue line is obtained. The slope of the blue line is $l_r = (j_c - j_{\text{sub},r})/(i_c - i_{\text{sub},r})$ and $\vartheta_r = \text{atan}(l_r)$. $\vartheta_r \in (0, \pi/2)$ is the inclination angle of blue line. There are also two scenarios.

Case 3: $\pi/4 < \vartheta_r \leqslant \pi/2$. The range profile should be extracted along each row j and can be obtained as $u[\text{round}(i_2), j]$. $i_2 = (j - j_c)/l_r + i_c$.

Case 4: $0 < \vartheta_r \leqslant \pi/4$. The range profile can be extracted along each column i and can be written as $u[i, \text{round}(j_2)]$. $j_2 = l_r(i - i_c) + j_c$. Thus, the range resolution can be defined as

$$\begin{cases} \rho_r = n_r\sqrt{d_r^2 + (d_a/l_r)^2}, & \text{Case 3} \\ \rho_r = n_r\sqrt{d_a^2 + (l_r d_r)^2}, & \text{Case 4}. \end{cases} \tag{52}$$

Equations (51) and (52) give the azimuth and range resolution calculation formula for squinted SAR, which is completely different from (50).

C. Geometric Position

The geometric position refers to the peak position of the impulse response in the 2-D image space. This parameter is generally used for geometric calibration. This article mainly analyzes the position of the point target in the focused image under different reference geometries. From the analysis in Section III, it can be seen that the target P is focused at position (x_0, r_0) after the EWD and CWD processing, and the data are aligned to its ZD position. The position of the target in the focused image is centered on $r_{\text{ref}} \tan\theta_c$, which may cause the image to shift in azimuth. This problem can be uniformly compensated by multiplying the phase $\exp(jk_x r_{\text{ref}} \tan\theta_c)$. Finally, target will be focused at the location $(x_0 - r_{\text{ref}} \tan\theta_c, r_0)$. In (1), the squint angle θ changes with the nearest slant range r_0, which makes the geometric deformation of the image after the SWD. The target was focused on position $(x_0 - r_0 \tan\theta_c, r_0/\cos\theta_c)$. After the tilt correction of (44), the target is focused to $(x_0 - r_{\text{ref}} \tan\theta_c, R_0)$ in the AD geomerty.

Position bias is a commonly used evaluation index. The position bias of a point target is simply defined as the Euclidean distance between the location of the maximum amplitude L_{image}

TABLE I
SAR SYSTEM PARAMETERS

Parameter	Value	Unit
Carrier frequency	10	GHz
Pulse duration	2	us
Bandwidth	500	MHz
Sampling frequency	750	MHz
Azimuth Antenna length	1	m
PRF	410	Hz
Effective velocity	60	m/s
The whole acquisition interval	27	s
Squint angel	50	degree
Center slant range	10	km
Height	4	km

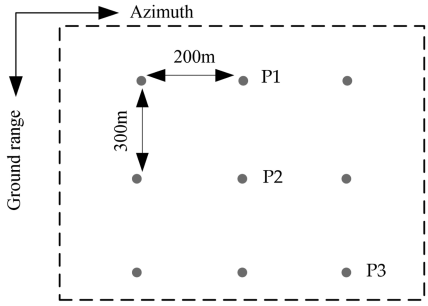

Fig. 7. Designed imaged area.

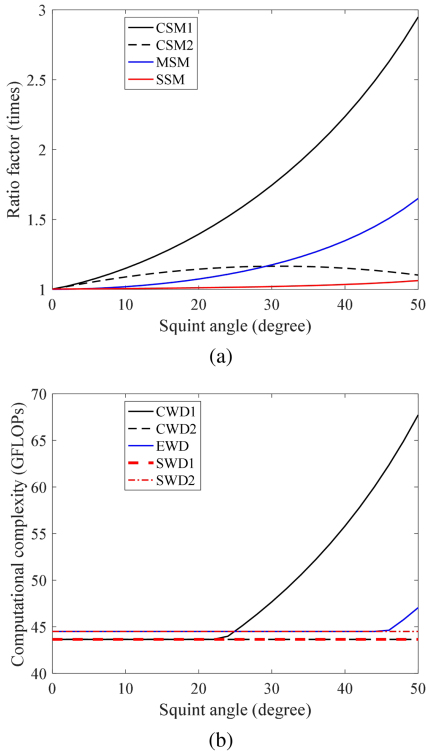

Fig. 8. Variation of ratio factor and computational complexity with the squint angle. (a) Ratio factor. (b) Computation complexity.

in the SAR image of a point target and the theoretical position $L_{\text{theoretical}}$ of that target, as follows:

$$L = \left| L_{\text{image}} - L_{\text{theoretical}} \right|. \tag{53}$$

V. EXPERIMENT RESULTS

Imaging results on simulated raw data are employed to validate the theoretical analysis and evaluate the performance of the three algorithms. The simulation parameters are listed in Table I. The designed imaged scene including nine point targets is shown in Fig. 7. Point P2 represents the center of the scene.

A. Computational Complexity

It can be seen from the analysis in Sections III and IV that interpolation is required according to the width of mapped range spectrum, otherwise full-resolution image will not be obtained. The computational complexity of different algorithms is mainly determined by the ratio factor defined in (36). Therefore, the change of ratio factor is first analyzed. According to (26), (27), (29), and (35), the variation of ratio factor with squint angle under various mappings is calculated, as shown in Fig. 8(a). Obviously, in the case of broadside or small squint systems, the ratio factor of each mapping is close to 1. With the increase of squint angle, the ratio factor corresponding to (26) increases rapidly and reaches about 3 times at 50 degrees, while the ratio factor corresponding to (27) changes relatively slowly and less than 1.2 times. In the following simulation experiments, we will point out that the wider range interpolation of (26) is unnecessary, and the effective spectrum corresponding to (27) can meet the requirements of full-resolution imaging. The ratio factor corresponding to MSM increases to about 1.6 times at 50°. The ratio factor corresponding to SSM is the smallest and always less than 1.2 times.

According to (37), when the ratio factor is less than the range oversampling factor, extension-interpolation is not required. For the actual echo, a certain oversampling will be set in the range direction and the oversampling rate is usually greater than 1.2. In the simulation, the range oversampling factor is set to 1.5. Therefore, within 0 to 50° squint angle, the CSM2 and SSM do not need to expand the number of interpolation points, but only need to consider the offset from the center range wavenumber. Assuming the number of input echoes samples M=11 200, N=12 700, and the interpolator length S_{ker} = 8, then the computational loads of three algorithms, measured in Giga-FLOPs are ploted as function of squint angle in Fig. 8(b). Here, five cases are considered: CWD1 (corresponding to CSM1), CWD2 (corresponding to CSM2), EWD, SWD1 (without geometric correction), SWD2 (with geometric correction). As shown in Fig. 8(b), the computational complexity of CWD2 is the same as that of SWD1, and the geometric correction operation of SWD2 increase the limited complexity. When the squint angle is less than 45°, EWD does not need range extension interpolation, and its complexity is consistent with that of SWD1. When the squint angle is greater than 45°, the complexity of EWD is higher than that of CWD2 and SWD1. However, as the squint angle increases, the computational burden of CWD1 increases significantly. In a word, CWD2 and SWD do not need to carry out range expansion-interpolation under 50° squint angle, and

TABLE II
IMAGING PARAMETERS ON THE SIMULATED TARGETS

Method	Targets	Azimuth			Range		
		Res (m)	PSLR (dB)	ISLR (dB)	Res (m)	PSLR (dB)	ISLR (dB)
Theoretical		0.5000	−13.26	−9.80	0.2656	−13.26	−9.80
CWD1	P1	0.4980	−13.28	−10.39	0.2638	−13.26	−9.96
	P2	0.4951	−13.41	−10.45	0.2526	−13.35	−9.93
	P3	0.4980	−13.40	−10.40	0.2646	−13.26	−9.96
CWD2	P1	0.5009	−13.28	−10.16	0.2662	−13.26	−9.91
	P2	0.5010	−13.30	−10.19	0.2619	−13.31	−9.93
	P3	0.5005	−13.28	−10.19	0.2664	−13.27	−9.96
EWD	P1	0.4961	−13.28	−10.22	0.2652	−13.36	−9.96
	P2	0.5017	−13.28	−10.25	0.2643	−13.36	−9.96
	P3	0.4987	−13.28	−10.19	0.2671	−13.38	−9.99
SWD	P1	0.4975	−13.32	−10.43	0.2655	−13.27	−9.91
	P2	0.4980	−13.35	−10.52	0.2655	−13.26	−9.91
	P3	0.4982	−13.30	−10.28	0.2655	−13.27	−9.91

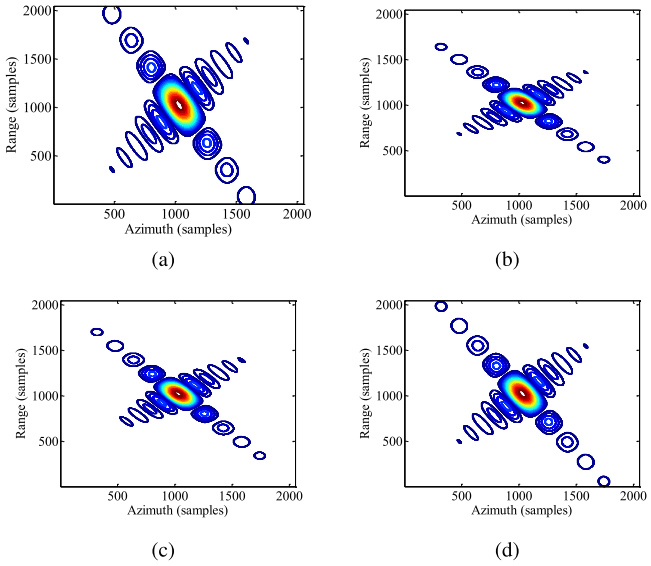

Fig. 9. Contour plots of impulse response function of target P3. (a) CWD1. (b) CWD2. (c) EWD. (d) SWD2. The dynamic range of contours is −40 dB–0 dB.

their computational complexity is the lowest. Except for CWD1, there is no big difference in the computational complexity of other cases.

B. Image Quality

First, in order to evaluate the focusing quality of different algorithms, three targets P1, P2, and P3 in Fig. 7 were evaluated and the evaluation results obtained by the proposed evaluation means are listed in Table II. Moreover, the 2-D contour plots of impulse response function of target P3 are presented in Fig. 9. It should be pointed out that since different algorithms have different range sample points and sampling interval, the 2-D contour plots differ somewhat. But essentially, they are the same in meters. Obviously, the results are consistent with the theoretical values, which shows that all three algorithms can achieve effective focusing of 50° squint angle. Besides, the results verify the effectiveness of the proposed evaluation method and the correctness of the resolution calculation formula of (51) and (52). Error results are obtained when the resolution is calculated by the broadside approach [corresponding to (50)]. Therefore, we can conclude that all three algorithms can achieve good focusing effects if full-resolution interpolation is performed. At the same time, it is unnecessary to interpolate in a wider range according to CSM1, and the width of CSM2 can already achieve full-resolution imaging.

Then, to better understand the mapping relationship, Fig. 10 displays the 2-D spectrum of raw data after different processing steps in Fig. 5. Fig. 10(a) shows the 2-D spectrum of echo before mapping, and its shape is similar to Fig. 3(a). It can be seen from Fig. 10(b) that there is a skewing in the spectrum after the CSM1, and the number of range sampling points increases from 12 000 to nearly 40 000. However, the actual effective spectrum is distributed in the middle of about 10 000 samples, and there are a large range of invalid sampling points. As shown in Fig. 10(c), CSM2 uses N points for interpolation, which has met the requirements of full resolution imaging. These conclusions confirm our analysis again. Fig. 10(d) and (e) illustrates there is no skewing in the spectrum after the MSM and the range sampling points is about 13 000, but the spectrum becomes skewing after ac operation. This validates the analysis in Section III that the ac term is the main factor causing the spectral distortion. Similarly, looking at Fig. 10(f) and (g), it is apparent that there is no skewing in the spectrum after the SSM, and the number of sampling points is N points. Interestingly, with the geometric correction as shown in (42), the spectrum becomes skewing again. This indicates that the target has been realigned to the orthogonal position after geometric correction. In addition, the effective spectrum of the signal is compressed between 60 000 and 11 000, about $\cos\theta_c$ times.

C. Geometric Position

Considering that we are mainly concerned about the actual position and theoretical position of the target, we use the gray image in the range of −80 dB–0 dB to display the focusing

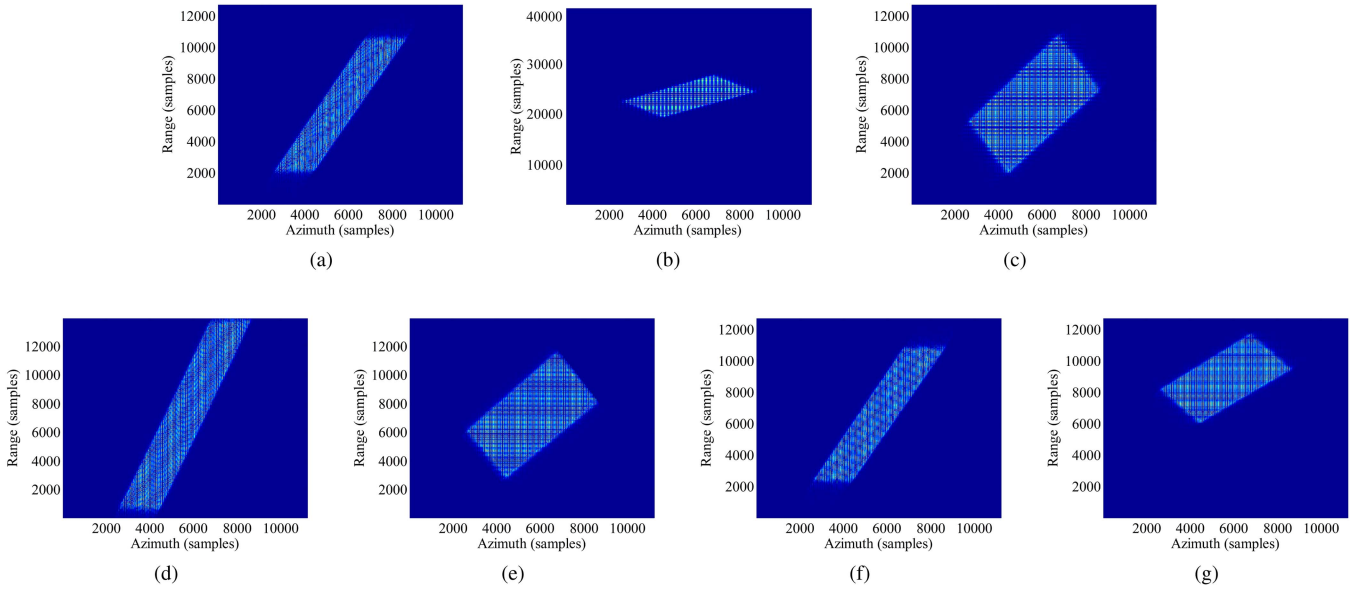

Fig. 10. 2-D spectra of the raw data. (a) Before mapping. (b) After the CSM1. (c) After the CSM2. (d) After the MSM in the EWD algorithm. (e) After ac in the EWD algorithm. (f) After the SSM in the SWD algorithm. (g) After geometric correction in the SWD algorithm.

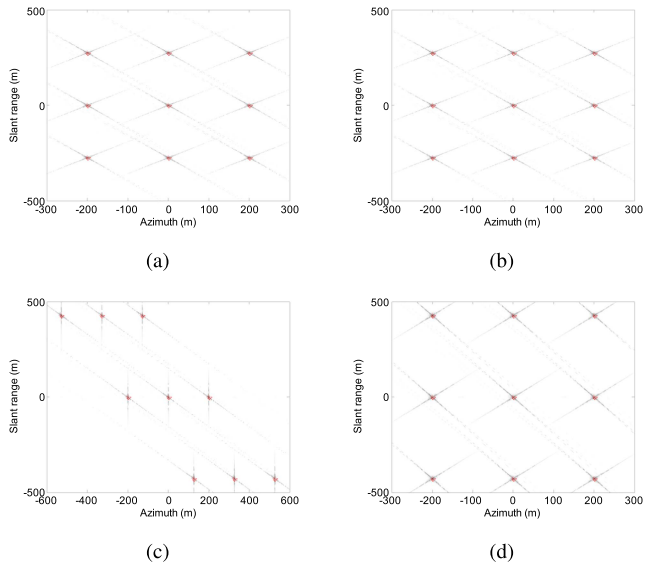

Fig. 11. Results using different algorithms. (a) CWD. (b) EWD. (c) SWD. (d) SWD with geometric correction.

TABLE III
GEOMETRIC POSITION BIAS OF TARGETS

Figure	P1	P2	P3
(a)	(0.07,0)	(0.07,0)	(0,0.06)
(b)	(0.07,0)	(0.07,0)	(0,0.06)
(c)	(0.07,0)	(0.07,0)	(0,0.1)
(d)	(0.07,0)	(0.07,0)	(0,0.1)

results, and use the "*" symbol to represent the theoretical position. The results are shown in the Fig. 11. In order to visualize the target position, the imaging results centered on the scene center target are shown. Here, CWD refers to CWD2. Since the results of CWD1 and CWD2 are consistent, only the result of CWD2 is given. It is apparent that all targets are focused near their corresponding theoretical position. As can be seen from Fig. 11(a) and (b), the targets are focused on the ZD geometry after the CWD and EWD processing. As shown in Fig. 11(c), the targets are focused on the AD geometry and the image has a geometric deformation after the SWD processing. In Fig. 11(d), the tilt of the image along the azimuth is eliminated after geometric correction.

Furthermore, the geometric position biases of the three targets are presented in Table III. Values in the Table are in meters. The range and azimuth sampling intervals are 0.18 m and 0.15 m, respectively. All targets are focused around the theoretical value, and the error is within one sampling unit. Since it is also uniformly sampled on the AD geometry, the actual digital image after the geometric correction is consistent with that of ZD processing. These results again validate the analysis of SWD in Section III.

Finally, to further test the analysis presented in this article, an SAR real image (Haikou Meilan International Airport, Hainan, China) is used as the input radar cross section to generate SAR echo. The range bandwidth is 300 MHz, the sampling frequency is 360 MHz, and the PRF is 360 Hz. Other parameters are consistent with Table I. The resolutions are 0.5 m in range and 0.5 m in azimuth. In the simulation, the input image is a real complex image. Each cell of the complex image is treated as a point scatterer (this actually contains the target signal and noise). No additional noise was added during the simulation. Fig. 12 shows the focused results processed by the different algorithms. It can be seen from Fig. 12 that the images are focused well. Obviously, Figs. 12(c) and 11(c) present the same geometric distortion. After geometric correction, Fig. 12(d) becomes the same as

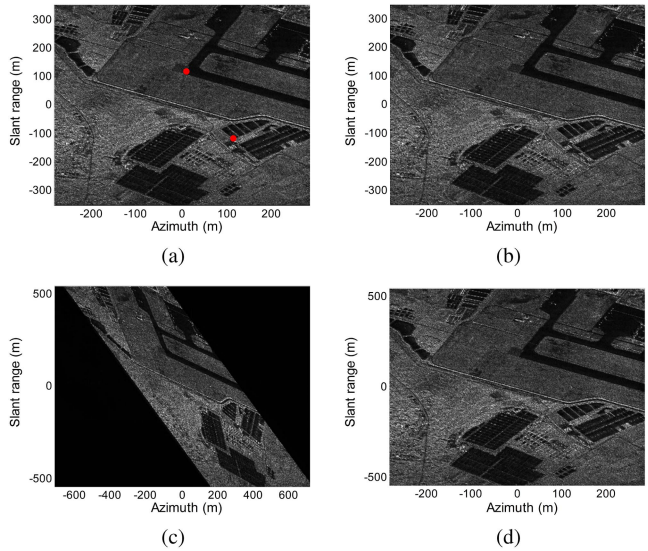

Fig. 12. Focused squinted SAR image. (a) CWD. (b) EWD. (c) SWD. (d) SWD with geometric correction.

Fig. 12(a), only the coordinate scale in the range direction is expanded by $1/\cos\theta_c$. We select two points corresponding to the red circle in Fig. 12(a). Taking the neighborhood of each point as a template, and using the normalized cross-correlation [34] as the similarity measure to search the template in Fig. 12(b) and (d), the coordinates of the corresponding points can be obtained. The results of coordinates show that the relative position offset is also within one sampling unit, which is consistent with the conclusion in Table III. Taken together, these results strongly proves the correctness of the analysis in this article.

VI. Conclusion

In this work, we first derive the 2-D wavenumber domain expression of squinted SAR in the ZD and AD geometries. Then, we analyze the internal connection of three commonly used wavenumber domain algorithms. On this basis, an evaluation system is established and the performance of the three algorithms is compared through experiments. Based on the analysis carried out in this article, we can get the following conclusions.

1) The AC term is the main factor that causes the spectrum skew after the CSM, and the MSM separates this term to reduce the skew effect. The SSM corresponds to the scale and skew transformations of the CSM. The focused image after SWD has azimuthal tilt, and the tilt effect can be corrected by phase multiplication in the RD domain. Both CWD and EWD focus targets on the ZD geometry, and SWD focuses targets on the AD geometry. The actual digital image obtained by SWD with geometric correction is consistent with the image processed by CWD and EWD.
2) The mapped effective spectrum needs to be calculated according to the range bandwidth B_r and azimuth bandwidth B_a, rather than the range sampling frequency and PRF. The number of interpolation points is determined by (37). When the squint angle is small, the difference in the computational burden of the three algorithms is small. Under 50° squint, when the range oversampling factor is set to be greater than 1.2 times, the CWD and SWD do not need to expand the number of sample points, and the computational complexity is equivalent. Generally, the computational complexity of EWD is greater than that of CWD and SWD.
3) All three algorithms can obtain well-focused images if full-resolution interpolation is performed, which overturns the conclusion in [23], [24], and [30] that CWD cannot effectively process squint data.

We believe that squinted mode in different platforms is a promising direction of further research in this area. Therefore, future work will aim to investigate the application of the wavenumber domain algorithm in spaceborne highly squinted SAR and airborne highly squinted SAR, to solve the range space variation problem and the motion compensation problem.

Acknowledgment

The authors would like to thank the anonymous reviewers for their valuable comments and suggestions which improved this article.

References

[1] F. He, Z. Dong, Y. Zhang, G. Jin, and A. Yu, "Processing of spaceborne squinted sliding spotlight and HRWS TOPS mode data using 2-D baseband azimuth scaling," *IEEE Trans. Geosci. Remote Sens.*, vol. 58, no. 2, pp. 938–955, Feb. 2020.
[2] J. Chen et al., "Blind NCS-based autofocus for airborne wide-beam SAR imaging," *IEEE Trans. Comput. Imag.*, vol. 8, pp. 626–638, Jul. 2022.
[3] J. Chen, M. Xing, H. Yu, B. Liang, J. Peng, and G.-C. Sun, "Motion compensation/autofocus in airborne synthetic aperture radar: A review," *IEEE Geosci. Remote Sens. Mag.*, vol. 10, no. 1, pp. 185–206, Mar. 2022.
[4] G. Sun, X. Jiang, M. Xing, Z. j. Qiao, Y. Wu, and Z. Bao, "Focus improvement of highly squinted data based on azimuth nonlinear scaling," *IEEE Trans. Geosci. Remote Sens.*, vol. 49, no. 6, pp. 2308–2322, Jun. 2011.
[5] G. W. Davidson, I. G. Cumming, and M. R. Ito, "A chirp scaling approach for processing squint mode SAR data," *IEEE Trans. Aerosp. Electron. Syst.*, vol. 32, no. 1, pp. 121–133, Jan. 1996.
[6] D. An, X. Huang, T. Jin, and Z. Zhou, "Extended two-step focusing approach for squinted spotlight SAR imaging," *IEEE Trans. Geosci. Remote Sens.*, vol. 50, no. 7, pp. 2889–2900, Jul. 2012.
[7] W. Xu, Y. Deng, P. Huang, and R. Wang, "Full-aperture SAR data focusing in the spaceborne squinted sliding-spotlight mode," *IEEE Trans. Geosci. Remote Sens.*, vol. 52, no. 8, pp. 4596–4607, Aug. 2014.
[8] D. Zhu et al., "An extended two step approach to high-resolution airborne and spaceborne SAR full-aperture processing," *IEEE Trans. Geosci. Remote Sens.*, vol. 59, no. 10, pp. 8382–8397, Oct. 2021.
[9] G. Zhang, Y. Liang, Z. Suo, and M. Xing, "Modified ERMA with generalized resampling for maneuvering highly squinted TOPS SAR," *IEEE Geosci. Remote Sens. Lett.*, vol. 19, Nov. 2022, Art. no. 4005405.
[10] M. Xing, Y. Wu, Y. D. Zhang, G.-C. Sun, and Z. Bao, "Azimuth resampling processing for highly squinted synthetic aperture radar imaging with several modes," *IEEE Trans. Geosci. Remote Sens.*, vol. 52, no. 7, pp. 4339–4352, Jul. 2014.
[11] X. Chen, T. Yi, F. He, Z. He, and Z. Dong, "An improved generalized chirp scaling algorithm based on lagrange inversion theorem for high-resolution low frequency synthetic aperture radar imaging," *Remote Sens.*, vol. 11, Aug. 2019, Art. no. 1874.
[12] A. Reigber et al., "Very-high-Resolution airborne synthetic aperture radar imaging: Signal processing and applications," *Proc. IEEE*, vol. 101, no. 3, pp. 759–783, Mar. 2013.
[13] A. Moreira, J. Mittermayer, and R. Scheiber, "Extended chirp scaling algorithm for air- and spaceborne SAR data processing in stripmap and ScanSAR imaging modes," *IEEE Trans. Geosci. Remote Sens.*, vol. 34, no. 5, pp. 1123–1136, Sep. 1996.

[14] Y. Wu, G.-C. Sun, X.-G. Xia, M. Xing, J. Yang, and Z. Bao, "An azimuth frequency non-linear chirp scaling (FNCS) algorithm for TOPS SAR imaging with high squint angle," *IEEE J. Sel. Topics Appl. Earth Observ. Remote Sens.*, vol. 7, no. 1, pp. 213–221, Jan. 2014.
[15] J. Chen, H. Kuang, W. Yang, W. Liu, and P. Wang, "A novel imaging algorithm for focusing high-resolution spaceborne SAR data in squinted sliding-spotlight mode," *IEEE Geosci. Remote Sens. Lett.*, vol. 13, no. 10, pp. 1577–1581, Oct. 2016.
[16] D. Li, G. Liao, W. Wang, and Q. Xu, "Extended azimuth nonlinear chirp scaling algorithm for bistatic SAR processing in high-resolution highly squinted mode," *IEEE Geosci. Remote Sens. Lett.*, vol. 11, no. 6, pp. 1134–1138, Jun. 2014.
[17] Z. Wang, M. Liu, G. Ai, P. Wang, and K. Lv, "Focusing of bistatic SAR with curved trajectory based on extended azimuth nonlinear chirp scaling," *IEEE Trans. Geosci. Remote Sens.*, vol. 58, no. 6, pp. 4160–4179, Jun. 2020.
[18] W. Wang, G. Liao, D. Li, and Q. Xu, "Focus improvement of squint bistatic SAR data using azimuth nonlinear chirp scaling," *IEEE Geosci. Remote Sens. Lett.*, vol. 11, no. 1, pp. 229–233, Jan. 2014.
[19] Z. Li, Y. Liang, M. Xing, Y. Huai, L. Zeng, and Z. Bao, "Focusing of highly squinted SAR data with frequency nonlinear chirp scaling," *IEEE Geosci. Remote Sens. Lett.*, vol. 13, no. 1, pp. 23–27, Jan. 2016.
[20] C. Cafforio, C. Prati, and F. Rocca, "SAR data focusing using seismic migration techniques," *IEEE Trans. Aerosp. Electron. Syst.*, vol. 27, no. 2, pp. 194–207, Mar. 1991.
[21] R. Bamler, "A comparison of range-doppler and wavenumber domain SAR focusing algorithms," *IEEE Trans. Geosci. Remote Sens.*, vol. 30, no. 4, pp. 706–713, Jul. 1992.
[22] A. Reigber et al., "Extended wavenumber-domain synthetic aperture radar focusing with integrated motion compensation," *IEE Proc. Radar Sonar Navigat.*, vol. 153, no. 3, pp. 301–310, Jul. 2006.
[23] M. Vandewal, R. Speck, and H. Süß, " Efficient and precise processing for squinted spotlight SAR through a modified Stolt mapping," *EURASIP J. Adv. Signal Process.*, vol. 2007, Dec. 2006, Art. no. 59704.
[24] H. Lin, J. Chen, M. Xing, X. Chen, D. You, and G. Sun, "2-D frequency autofocus for squint spotlight SAR imaging with extended omega-K," *IEEE Trans. Geosci. Remote Sens.*, vol. 60, Jul. 2022, Art. no. 5211312.
[25] Y. Mo, H. Yan, and B. Zhao, "Novel approach based on deramping technique for squinted sliding spotlight SAR imaging," *J. Electron.*, vol. 30, no. 3, pp. 243–253, 2013.
[26] W. Liu, G. C. Sun, X. G. Xia, D. You, M. Xing, and Z. Bao, "Highly squinted MEO SAR focusing based on extended omega-K algorithm and modified joint time and doppler resampling," *IEEE Trans. Geosci. Remote Sens.*, vol. 57, no. 11, pp. 9188–9200, Nov. 2019.
[27] G. Fornaro, E. Sansosti, R. Lanari, and M. Tesauro, "Role of processing geometry in SAR raw data focusing," *IEEE Trans. Aerosp. Electron. Syst.*, vol. 38, no. 2, pp. 441–454, Apr. 2002.
[28] G. Fornaro, G. Franceschetti, and S. Perna, "Motion compensation of squinted airborne SAR raw data: Role of processing geometry," in *Proc. Int. Geosci. Remote Sens. Symp.*, Anchorage, AK, USA, 2004, pp. 1518–1521.
[29] G. Ping et al., "Improved focusing approach for highly squinted beam steering SAR," *IET Radar Sonar Navigat.*, vol. 10, no. 8, pp. 1394–1399, 2017.
[30] T. Xiong, M. Xing, X. G. Xia, and Z. Bao, "New applications of omega-K algorithm for SAR data processing using effective wavelength at high squint," *IEEE Trans. Geosci. Remote Sens.*, vol. 51, no. 5, pp. 3156–3169, May 2013.
[31] G. W. Davidson and I. Cumming, "Signal properties of spaceborne squint-mode SAR," *IEEE Trans. Geosci. Remote Sens.*, vol. 35, no. 3, pp. 611–617, May 1997.
[32] I. G. Cumming and F. H. Wong, *Digital Signal Processing of Synthetic Aperture Radar Data: Algorithms and Implementation*. Norwood, MA, USA: Artech House, 2005.
[33] T. Xiang, D. Zhu, and F. Xu, "Processing of ultra-high resolution spaceborne spotlight SAR data based on one-step motion compensation," in *Proc. Int. Geosci. Remote Sens. Symp.*, Valencia, Spain, 2018, pp. 8933–8936.
[34] R. Feng, H. Shen, J. Bai, and X. Li, "Advances and opportunities in remote sensing image geometric registration: A systematic review of state-of-the-art approaches and future research directions," *IEEE Geosci. Remote Sens. Mag.*, vol. 9, no. 4, pp. 120–142, Dec. 2021.

Xing Chen was born in Yunnan Province, China, in 1993. He received the B.S. and M.S. degrees in information engineering in 2017 and 2019, respectively, form the National University of Defense Technology, Changsha, China, where he is currently working toward the Ph.D. degree in information and communication engineering.

His major research interests are SAR system design, imaging, and signal processing.

Zhenyu Hou was born in Shandong, China, in May 1993. He received the M.S. degree in information and communication engineering in 2017 from the National University of Defense Technology (NUDT), Changsha, China, where he is currently working toward the Ph.D. degree in information and communication engineering.

His major research interests are spaceborne SAR imaging and signal processing.

Zhen Dong was born in Anhui, China, in September 1973. He received the Ph.D. degree in electrical engineering from the National University of Defense Technology (NUDT), Changsha, China, in 2001.

He is currently a Professor with the College of Electronic Science and Engineering, NUDT. His recent research interests include SAR system design and processing, ground moving target indication (GMTI), and digital beamforming (DBF).

Zhihua He was born in Sichuan, China, in September 1982. He received the Ph.D. degree in electrical engineering from the National University of Defense Technology (NUDT), Changsha, China, in 2011.

He is currently an Associate Professor with the College of Electronic Science and Technology, NUDT. His recent research interests include SAR system design and processing, video SAR, and subsurface imaging radar.